#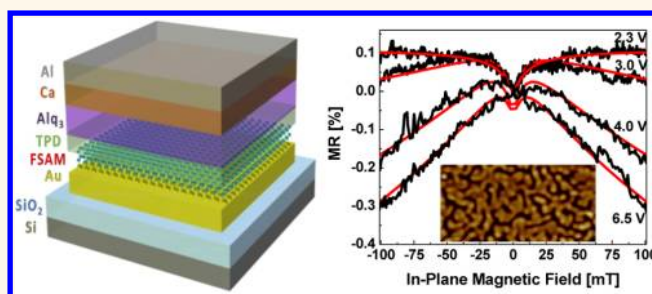 Interface Engineering To Control Magnetic Field Effects of Organic-Based Devices by Using a Molecular Self-Assembled Monolayer

Hyuk-Jae Jang,[†,‡,*] Sujitra J. Pookpanratana,[†] Alyssa N. Brigeman,[‡] R. Joseph Kline,[§] James I. Basham,[†] David J. Gundlach,[†] Christina A. Hacker,[†] Oleg A. Kirillov,[†] Oana D. Jurchescu,[‡] and Curt A. Richter[†,*]

[†]Semiconductor and Dimensional Metrology Division, National Institute of Standards and Technology, 100 Bureau Drive, Gaithersburg, Maryland 20899, United States, [‡]Department of Physics, Wake Forest University, 1834 Wake Forest Road, Winston-Salem, North Carolina 27109, United States, and [§]Materials Science and Engineering Division, National Institute of Standards and Technology, 100 Bureau Drive, Gaithersburg, Maryland 20899, United States

ABSTRACT Organic semiconductors hold immense promise for the development of a wide range of innovative devices with their excellent electronic and manufacturing characteristics. Of particular interest are nonmagnetic organic semiconductors that show unusual magnetic field effects (MFEs) at small subtesla field strength that can result in substantial changes in their optoelectronic and electronic properties. These unique phenomena provide a tremendous opportunity to significantly impact the functionality of organic-based

devices and may enable disruptive electronic and spintronic technologies. Here, we present an approach to vary the MFEs on the electrical resistance of organic-based systems in a simple yet reliable fashion. We experimentally modify the interfacial characteristics by adding a self-assembled monolayer between the metal electrode and the organic semiconductor, thus enabling the tuning of competing MFE mechanisms coexisting in organic semiconductors. This approach offers a robust method for tuning the magnitude and sign of magnetoresistance in organic semiconductors without compromising the ease of processing.

KEYWORDS: organic semiconductors · magnetic field effects · magnetoresistance · interface engineering · molecular self-assembled monolayers

Organic semiconductors provide a route to revolutionary changes in many areas of device technology with their unique electronic properties and functionalities, which can be easily tailored by chemical synthesis and molecular engineering.[1−5] Among the most intriguing properties are the magnetic field effects (MFEs) of organic semiconductors.[6,7] Although the fundamental mechanisms of MFEs are not yet fully understood, the MFEs offer an innovative means to develop new organic-based devices and provide a novel experimental platform to improve the understanding of dynamic processes of charge carrier transport in organic materials.[6−10] The full utilization of organic MFEs in device applications is contingent on the ability to tune the MFEs, preferably by a simple manufacturable process. To date, this has been achieved by making significant structural alterations to devices such as adding a thick insulating layer, varying organic layer thickness, blending materials, or invasive annealing, which can limit the reliable, high volume, yet low-cost device production capability.[11−15] In this report, we demonstrate for the first time that self-assembled monolayers (SAMs) can also be used in tuning MFEs. We present a simple method to change MFEs in a reliable fashion by using fluorinated SAMs to modify interfacial properties.

Several reports show that the interfaces between two different materials such as metal/organic, dielectric/organic, and organic/organic play a critical role in determining the performance and operation of organic-based devices by controlling charge carrier injection and transport mechanisms.[16−18] The insertion
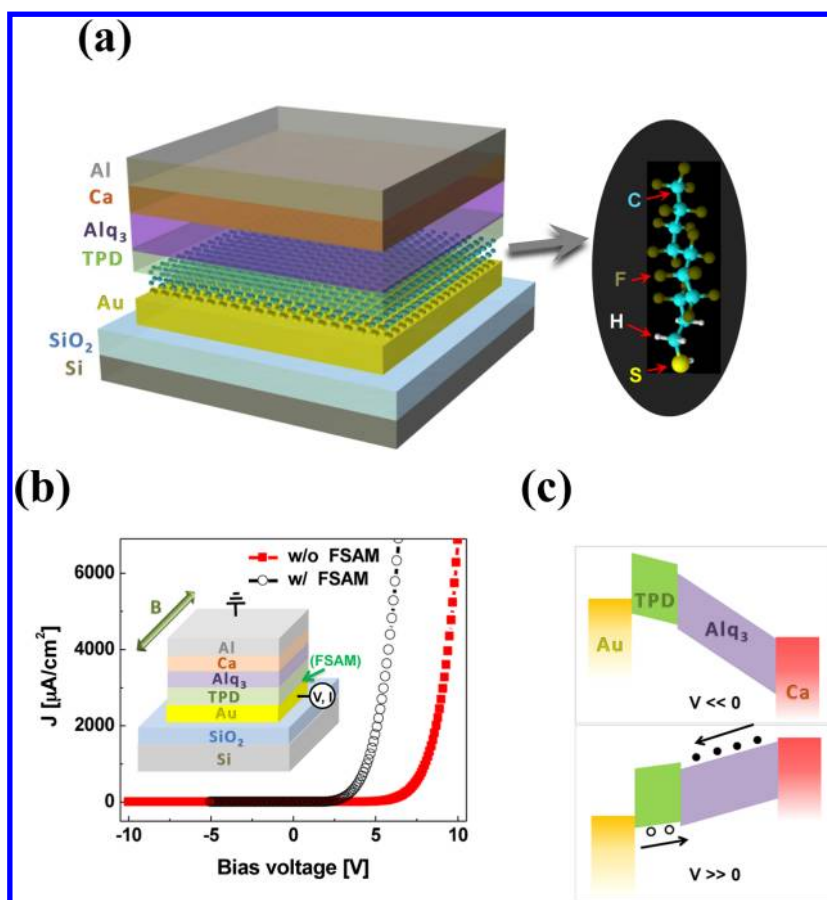
Figure 1. Device structure and electrical characteristics of the Au/TPD/Alq$_3$/Ca system. (a) Illustration of Au/TPD/Alq$_3$/Ca device structure with fluorinated-SAM (F-SAM) treatment and the molecular structure of F-SAM (heptadecafluoro-1-decanethiol [CF$_3$(CF$_2$)$_7$(CH$_2$)$_2$SH]). (b) Inset: illustration of the electrical and magnetic field measurements setups. Current density–bias voltage ($J–V$) plots of the systems; black open circles correspond to the device with F-SAM, and red filled squares represent the device without F-SAM. (c) Illustration of current rectification in the system with simplified band diagrams at negative (top image) and positive (bottom) bias voltages.

of a SAM between an electrode and an organic semiconductor has long been used to manipulate interfacial properties.[19,20] SAMs are molecular assemblies, formed spontaneously on an inorganic solid surface by chemisorption of molecular constituents in solution or gas phase, and they are known to offer simple fabrication processes for the interface and surface modification of organic-based systems.[19−22] Exploiting this unique characteristic of SAMs, we developed a novel method of altering the MFE on electrical resistance of organic-based devices by simply inserting a SAM between a metal electrode and an organic semiconductor. The MFE on electrical resistance of organic semiconductors, namely, organic magnetoresistance (MR), was first found in an organic light-emitting diode (OLED) made of electron- and hole-transporting bilayer structure.[7,9,10] We built a similar bilayer system composed of Alq$_3$ [tris(8-hydroxyquinoline)aluminum] and TPD [N,N′-bis(3-methylphenyl)-N,N′-diphenylbenzidine], and we treated a metal electrode, Au with fluorinated SAM (heptadecafluoro-1-decanethiol [CF$_3$(CF$_2$)$_7$(CH$_2$)$_2$SH] or F-SAM) to alter the MFE mechanisms in the system. We show that the F-SAM treatment switches the polarity of

MR in a low bias voltage regime, and this further leads to the realization of the variable MR operated by an external bias voltage. In order to develop a detailed understanding of how the interfacial modification by the F-SAM affects the MFE mechanisms, we carried out a series of physical and electrical measurements of the TPD/Alq$_3$ bilayer systems as well as single Alq$_3$ layer structures. We propose that enhanced charge trapping and accumulation at interfaces induced by the insertion of F-SAM is the main source for the changes in MFE mechanisms resulting in a sign reversal of MR.

RESULTS AND DISCUSSION

Our TPD/Alq$_3$ bilayer system is schematically illustrated in Figure 1a along with the electrical and magnetic measurement geometry in the inset of Figure 1b. Two different types of devices, one without and the other with an F-SAM between the Au electrode and the TPD layer, were constructed to clarify the effect of interfacial modification by F-SAM on the MR. Details of the fabrication process are documented in the Experimental Methods. Alq$_3$ and TPD are widely studied materials that are used for organic electronic and
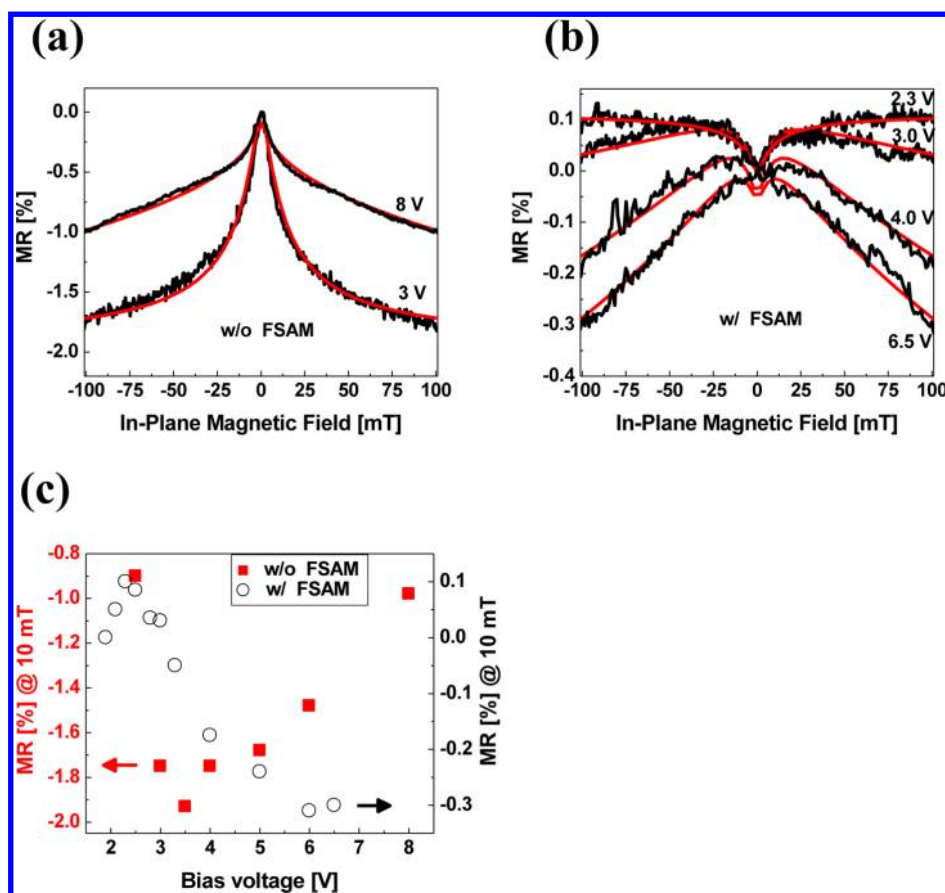
Figure 2. Magnetoresistance of the Au/TPD/Alq₃/Ca structures with and without F-SAM treatment on Au. (a) Magneto-resistance plots of the devices without F-SAM measured at room temperature with a bias voltage of 3.0 and 8.0 V (black lines). (b) Magnetoresistance plots of the devices with an F-SAM measured at room temperature with a bias voltage of 2.3, 3.0, 4.0, and 6.5 V (black lines). All the data were fitted with a combined model of empirical non-Lorentzian and √B dependence (red lines). (c) Bias voltage dependence of magnetoresistance of the devices with (black open circles) and without (red filled squares) F-SAM.

optoelectronic applications serving as electron- (Alq₃) and hole (TPD)-transporting layers.[9,23,24] Current density−voltage (J−V) curves of the Au/TPD/Alq₃/Ca devices (without and with an F-SAM) display current rectifying behaviors, as shown in Figure 1b, which are common in OLED structures.[23,24] This is because efficient charge injection into (or collection from) organic layers was ensured by Au (hole-injecting) and Ca (electron-injecting) electrodes as illustrated in Figure 1c with simplified band diagrams.[4,5,16,23] Ultraviolet photoelectron spectroscopy (UPS) data indicate that F-SAM treatment raises the work function of Au by ≈0.5 eV, which may produce more efficient hole injection (see Figure S3, Supporting Information).[4,23,24]

Figure 2a displays the MR curves measured on the Au/TPD/Alq₃/Ca system without an F-SAM under two different constant bias voltages. Even though both graphs show the reduction of electrical resistance under the increase of an external magnetic field (negative MR or −MR), their shape is quite different at low (3 V) and high (8 V) bias voltages. In the low bias voltage regime (<5 V), the MR curves were well fit with the empirical non-Lorentzian model, $B^2/(B_0 + |B|)^2$,

where B is the applied magnetic field and B_0 has been suggested to be related to the hyperfine field strength (see Supporting Information).[7,25] However, the MR curves in the higher voltage regime cannot be well fit with the same model, especially at higher magnetic fields. This implies that at least two different MFE mechanisms contribute to the MR in our TPD/Alq₃ systems, depending on the magnitude of bias voltage and magnetic field; one MFE mechanism dominates at low bias voltages over the whole magnetic field range investigated here (up to ≈100 mT), and then another becomes stronger as a bias voltage increases, even at a lower magnetic field. The high magnetic field response appears to be proportional to the square root of B. Similar high field √B behavior was previously observed in the MR of other organic systems, but its origin is debated.[13,26,27] In addition, the high field √B behavior was observed in MR of strongly disordered inorganic electronic systems due to the delocalization of charge carriers[28] and also in the chemical reaction change induced by the difference in gyromagnetic factors (g-factors) of electron−hole radical pairs.[29] We will further discuss its physical origin later in this report.
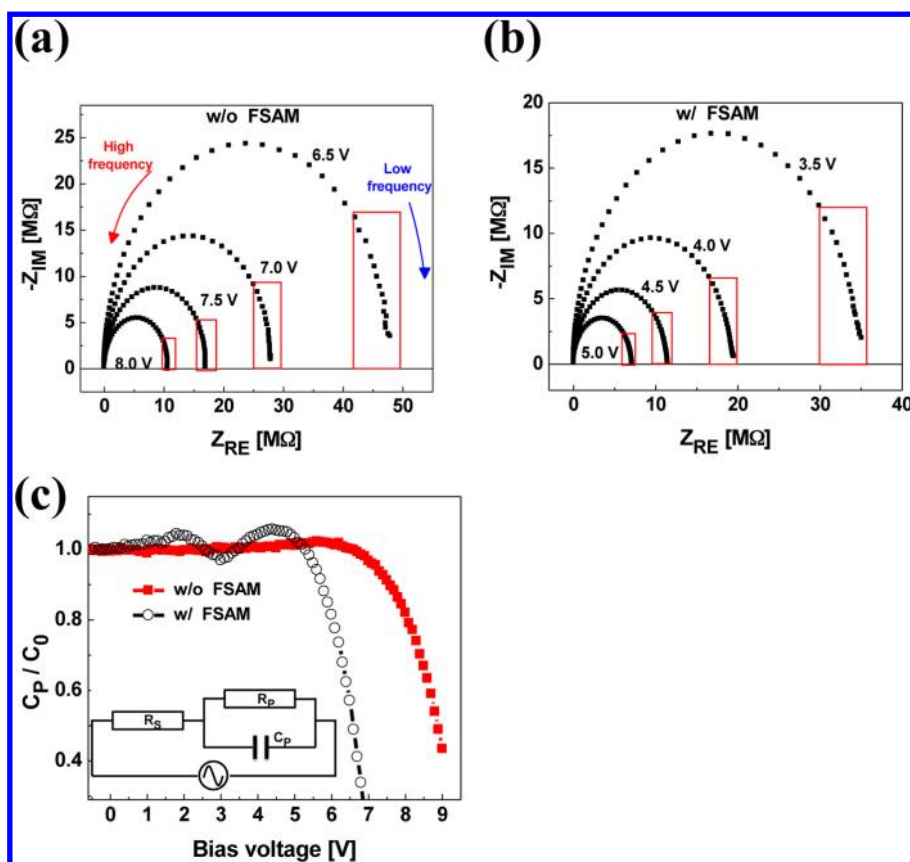
Figure 3. Impedance and capacitance−voltage spectroscopy results of the Au/TPD/Alq₃/Ca structures with and without F-SAM. Cole−Cole plots of the device (a) without F-SAM and (b) with F-SAM at various bias voltages, and the regimes of red rectangles display a slight deviation off a semicircle in the system with F-SAM. (c) Inset: illustration of a parallel resistor−capacitor (R_P−C_P) circuit in series with a resistor (R_S). The normalized capacitance (C_P/C_0) *versus* bias voltage of the systems with F-SAM (open black circles) and without F-SAM (filled red squares) measured at 107 Hz at room temperature. C_0 was ≈12 pF for the system with F-SAM and ≈13 pF for the one without F-SAM.

By taking the $\sqrt{B}$ dependence into account, we were able to fit the MR data with a combined model, $a_0 \times B^2/(B_0 + |B|)^2 + b_0 \times (|B|/B_1)^{0.5}$, as illustrated in Figure 2a, where a_0 and b_0 can be considered as weighted coefficients representing the relative contributions between the two different mechanisms inducing the organic MR and B_1 is a constant representing the strength of source causing $\sqrt{B}$ behavior.

When an F-SAM was inserted between the Au electrode and the TPD layer, the behavior of MR became much more intriguing as shown in Figure 2b; we have engineered the devices such that they have a variable MR polarity regulated by an external bias voltage. This remarkable bias-voltage-controlled MR polarity was enabled due to a sign reversal of MR in a lower bias voltage regime with respect to the system without an F-SAM. While the MR of these devices is tunable *via* the dramatic voltage dependence, all the data are well-described by the combined non-Lorentzian and $\sqrt{B}$ dependence model. The voltage dependence of MR of both TPD/Alq₃ systems without and with an F-SAM is summarized in Figure 2c.

Impedance and low-frequency ac capacitance−voltage (C−V) spectroscopies are powerful tools for characterizing the electrical properties of materials and their interfaces, and they have been extensively used for analyzing the charge carrier injection and transport of OLED structures.[30−34] These spectroscopies provided us a better understanding of the changes induced in the electrical properties of our TPD/Alq₃ systems when an F-SAM was inserted. The equivalent circuit of a typical OLED structure can be described by a parallel resistor−capacitor (R_P−C_P) circuit in series with a resistor (R_S), as illustrated in the inset of Figure 3c.[30,31] The R_S represents the contribution of the electrodes' contact resistance to the organic layer.[30,31] In a simple system having both R_P and C_P independent of the frequency, the Cole−Cole plot, which describes the relation between the real and imaginary parts of the impedance of the system at a given bias voltage, should display a semicircle in its shape.[30,31] We measured the impedance of devices with and without an F-SAM in the frequency range of 20 Hz through 200 kHz at various bias voltages and found that the Cole−Cole plots of both devices show generally semicircular patterns as described in Figure 3a,b. However, the device containing an F-SAM shows a slight deviation from the semicircle tailing out in the low-frequency
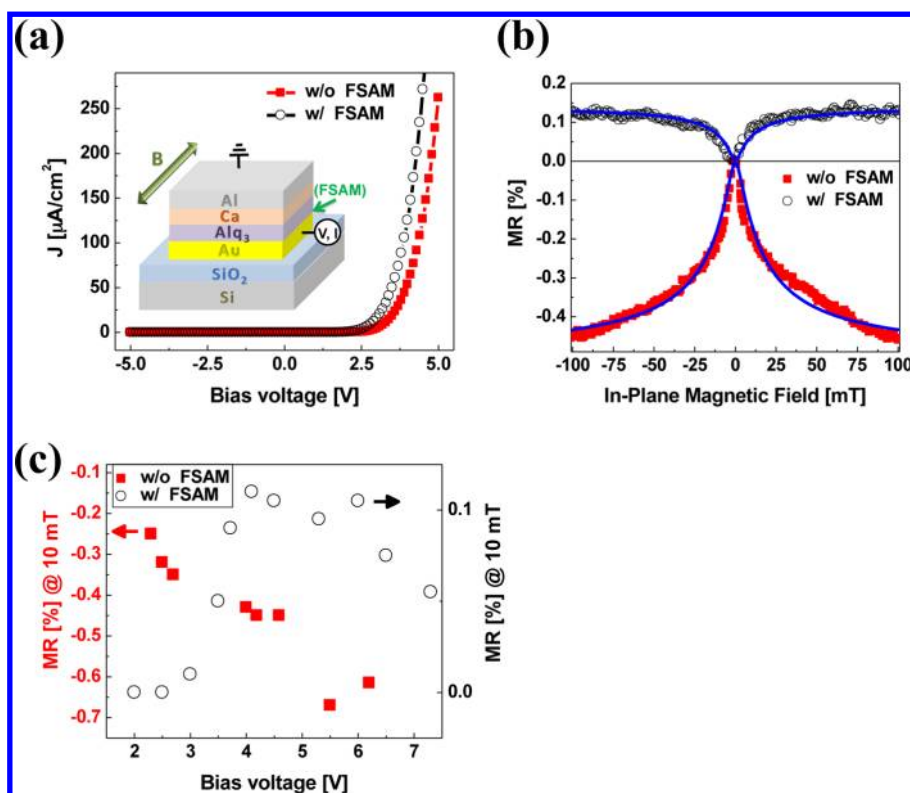
Figure 4. Electrical and magnetoresistance characteristics of the Au/Alq$_3$/Ca structures with and without F-SAM treatment on Au. (a) Inset: illustration of the device structure along with electrical and magnetic field measurements setups. Current density−bias voltage (J−V) plots of the systems. (b) Magnetoresistance plots of the devices measured with $J \approx 145\ \mu\text{A/cm}^2$ at room temperature and fit with empirical non-Lorentzian model (blue lines). (c) Bias voltage dependence of magneto-resistance of the devices. In all the plots, black open circles correspond to the device with F-SAM and red filled squares represent the device without F-SAM.

range (from 20 to ≈200 Hz; right side of the semicircle). This low-frequency tail indicates that there may be interfacial polarization in addition to the bulk dielectric response from organic materials to the bias voltage.[30]

Low-frequency C−V spectroscopy provided further in-depth analysis of charge carrier injection and transport in our devices.[31−35] Figure 3c shows the normalized capacitance of the devices with and without an F-SAM at the frequency of 107 Hz. The capacitance of the device without an F-SAM is constant at low bias voltages, then shows a small increase followed by rapid decrease at higher voltage. The flat regime of the C−V spectroscopy is typical and represents the geometrical capacitance, C_0, which is directly related to the dielectric properties of the organic materials in the devices.[30−33] As the forward bias voltage increases, the injection of charge is initially dominated by majority carriers, and then the rapid drop of the capacitance follows when the injection of the minority carriers becomes significant.[30−33] This decrease of the capacitance can be attributed to the delayed response of space charges to the ac voltage.[36,37] The slight increase in the capacitance right before the sudden decrease implies the accumulation and trapping of charge carriers at an energetic barrier formed inside of the device.[31−33] This energetic barrier is most likely

located at the TPD/Alq$_3$ interface due to slight band misalignment between TPD and Alq$_3$.[33]

The device with an F-SAM shows a more complex behavior (black open circles, Figure 3c); it displays two pronounced capacitance humps, indicating two different regions in the device that contain a stronger energetic barrier inducing charge carrier accumulation and trapping.[31−33]

In order to elucidate the origin of charge accumulation observed as a capacitance hump and its role on the change of MR, we investigated simpler structures made of a single Alq$_3$ layer. The structures are schematically described in the inset of Figure 4a. Figure 4a shows the J−V curves of Au/Alq$_3$/Ca devices, one with an F-SAM between Au and Alq$_3$ and the other without it. Although both devices display similar diode-like characteristics (since the electrodes are engineered for this current rectification behavior as explained earlier), we observed contrasting MR behaviors under constant applied voltages as illustrated in Figure 4b; when an F-SAM was inserted between the Au electrode and the Alq$_3$, the sign of MR was reversed from negative to positive, where a positive MR (+MR) represents an increased electrical resistance under the increase of an external magnetic field. Both negative and positive MR curves that are not as complex as
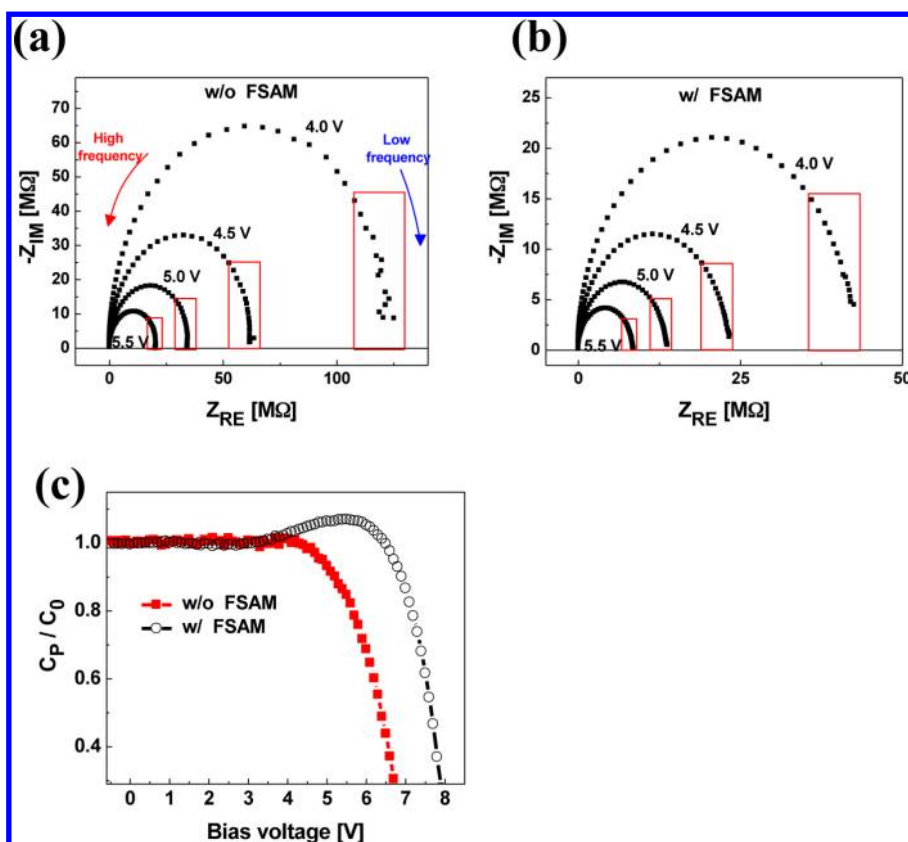
Figure 5. Impedance and capacitance−voltage spectroscopy results of the Au/Alq$_3$/Ca structures with and without F-SAM. (a) Cole−Cole plots of the device without F-SAM at various bias voltages. (b) Cole−Cole plots of the device with F-SAM at various bias voltages, and the regimes of red rectangles display a slight deviation off a semicircle in the system with F-SAM. (c) Normalized capacitance (C_P/C_0) *versus* bias voltage of the systems with F-SAM (open black circles) and without F-SAM (filled red squares) measured at 107 Hz at room temperature. C_0 was ≈16 pF for the system with F-SAM and ≈6 pF for the one without F-SAM.

those obtained in the TPD/Alq$_3$ samples and were fit well with a simple non-Lorentzian model at all bias voltages that we used. The MR sign of both Alq$_3$ systems without (−MR) and with an F-SAM (+MR) did not reverse over the entire bias voltage range investigated. The voltage dependence of MR is summarized in Figure 4c.

Impedance and low-frequency $C−V$ spectroscopy studies revealed further details of the charge carrier transport in the Au/Alq$_3$/Ca devices with and without an F-SAM. Similar to the Au/TPD/Alq$_3$/Ca systems, the Cole−Cole plot for the Au/Alq$_3$/Ca devices forms a semicircle as shown in Figure 5a. A small deviation in the low-frequency range occurs when an F-SAM was added between the Au and Alq$_3$ (Figure 5b), implying the existence of an interfacial polarization in the system as mentioned earlier.[30] The Au/Alq$_3$/Ca systems without and with an F-SAM also display a difference in the low-frequency $C−V$ spectroscopy as illustrated in Figure 5c; the $C−V$ curves of both systems have an initial flat region owing to the geometrical capacitance followed by a sudden decrease of the capacitance at higher bias voltage, but only the system with an F-SAM displayed an increase in capacitance immediately before the high bias capacitance drop, indicating the accumulation of charge carriers at an energetic barrier formed inside of the device as explained earlier.[31−33] It

is reasonable to envision that this energetic barrier is located at the interface between the Au and the Alq$_3$ where the F-SAM was inserted.[16]

SAMs are known to affect electronic properties in complex ways owing to their ability to change not only the electrostatic environment at critical interfaces but also the electronic structure through subtle modifications to film microstructure.[18−24] To gain further insights into how and why the insertion of F-SAM causes the charge carrier trapping and accumulation, we investigated the structural properties of Alq$_3$ thin films deposited on 100 nm thick Au layers with and without F-SAM surface treatment. First, in order to investigate the details of the thin film growth, we prepared the samples with two different thicknesses, 10 and 100 nm, of Alq$_3$ (see Experimental Methods). Figure 6b,e shows atomic force microscopy (AFM) images of 10 nm thick Alq$_3$ thin films on Au layers: one without and the other with an F-SAM. There is a stark difference in the topography of these two samples; without F-SAM treatment, the Alq$_3$ uniformly covers the entire Au area producing an almost feature-less morphology. In contrast, in samples with F-SAM treatment, the Alq$_3$ congregates into smaller areas due to spinodal dewetting,[38] showing a pattern of corrugation and islands. This noticeable topographical
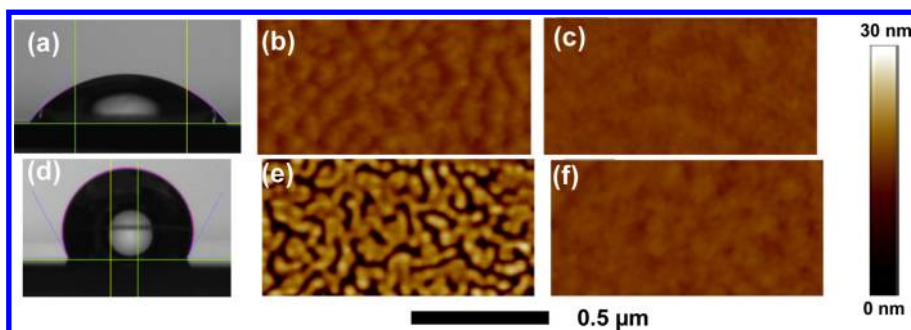
Figure 6. Water contact angle measurements and AFM data of Alq$_3$ thin films on untreated and treated Au with F-SAM. (a) Captured image for water contact angle measurements on untreated Au surface, and the measured contact angle was $54 \pm 3°$ (hydrophilic). (b) AFM data of $\approx$10 nm thick Alq$_3$ on untreated Au. Average roughness (R_a) was $\approx$0.7 nm. (c) AFM data of $\approx$100 nm thick Alq$_3$ on untreated Au. R_a was $\approx$0.35 nm. (d) Captured image for water contact angle measurements on F-SAM-treated Au surface, and the measured contact angle was $114 \pm 3°$ (hydrophobic). (e) AFM data of 10 nm thick Alq$_3$ on F-SAM-treated Au. R_a was $\approx$3.9 nm. (f) AFM data of 100 nm thick Alq$_3$ on F-SAM-treated Au. R_a was $\approx$0.45 nm.

difference between the two films likely results from the change in surficial characteristics of Au after F-SAM treatment. Ten nanometer thick TPD films on Au with F-SAM treatment also displayed much rougher topographical features than those without an F-SAM (Figure S4). Water contact angle measurements on the two different surfaces (Au layers with and without F-SAM treatment) confirmed the distinct difference in surficial characteristics, as shown in Figure 6a,d, indicating that the F-SAM treatment made the Au surface hydrophobic.[39] In contrast to the 10 nm thick Alq$_3$ films, when the thickness of the films increases to 100 nm, the morphological difference in topography disappears, as illustrated in Figure 6c,f; Alq$_3$ covered the Au film quite uniformly in both of these thick samples, suggesting that the Alq$_3$ morphology change by F-SAM treatment is strong only near the interface.[18] In addition, the X-ray diffraction (XRD) data display no substantial difference between the bulk crystalline structures of 100 nm thick Alq$_3$ films deposited on hydrophilic and hydrophobic Au surfaces; the films on both surfaces are either amorphous or composed of small crystals with random orientation (Figure S5). Since the diffraction measurement is the bulk average scattering, the data suggest that the interfacial effect on the film quickly diminishes after the first few nanometers. Thus, physical characterization indicates that a distinct morphology change occurs in the Alq$_3$ layer of our devices only near the F-SAM-treated Au electrode as compared to the untreated electrode. On the basis of our physical characterization results, we believe that disordered grain boundaries caused by distinct morphology changes in the organic layer (Alq$_3$ for the Alq$_3$-only devices and TPD for the TPD/Alq$_3$ devices) near the F-SAM-treated Au electrode is the main source for the carrier accumulation observed in the capacitance measurements.[40,41]

To further support our interpretation, we also investigated the Au/Alq$_3$/Ca system with the treatment of a different SAM, 16 mercaptohexadecanoic acid (HS(CH$_2$)$_{15}$CO$_2$H or MHA). Unlike F-SAM, MHA on Au is known to provide a very hydrophilic surface

(Figure S6a).[42,43] AFM measurements of a 10 nm thick Alq$_3$ thin film deposited on MHA-treated Au showed that the surface of Alq$_3$ is as smooth and uniform as that of Alq$_3$ directly on Au (Figure S6b). Magnetic field electrical measurements revealed that the Au/MHA/Alq$_3$/Ca system showed negative MR curves similar to the ones of the Au/Alq$_3$/Ca system, being well fit with non-Lorentzian model (Figure S6c). These data further confirm our findings that the observed alteration of organic MR is induced by the interfacial morphology change due to F-SAM treatment.

There are several theoretical proposals to explain the underlying physical mechanism causing organic MR including electron–hole pair, triplet–polaron interaction, and bipolaron models.[7,11–13,44–46] It has been suggested that the dominant mechanism(s) can vary depending on the choice of organic materials, operating conditions, and device structures[7,12] which may be the reason that there is no consensus on the fundamental physical mechanism. On the basis of our experimental observations, we conclude that the most likely dominant physical mechanism causing organic MR in our Au/Alq$_3$/Ca systems is the triplet–polaron interaction mechanism.[44,47] Triplet excitons reportedly have a much longer lifetime than their singlet counterparts, and thus their population in organic semiconductors has a strong influence on the electric current.[7,44,48] It has previously been shown that the triplets can interact with charge carriers in the following manner:[44,47]

$$T + D \leftrightarrow (T \cdots D) \rightarrow D + S \qquad (1)$$
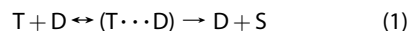
where T is the triplet state, D is the charge carrier, $(T \cdots D)$ is a pair state, and S is the singlet state. Equation 1 indicates that the triplet population may affect the electric current in opposite ways: when the scenario on the left side occurs, a larger triplet population can decrease the electric current because it induces more triplet charge carrier scattering, thus reducing charge carrier mobility. In contrast, when the situation corresponds to the right side, a larger triplet population can increase the electric current because triplets can be

quenched by trapped charges and dissociated into secondary charge carriers contributing to the electric current especially near the electrodes.[15,44,47] The triplet population can vary as a result of applying an external magnetic field; without an external magnetic field, singlet precursor pairs can intermix with entire triplet precursor states, T_{-1}, T_0, and T_1, through the intersystem crossing mainly due to random hyperfine field, but when an external magnetic field is applied, the degeneracy of the triplet states is lifted by Zeeman splitting and the mixing can occur only between singlets and T_0 triplets, thus decreasing triplet population.[9,11,15] Therefore, the triplet−polaron scattering (left side of eq 1) will generate a negative MR (−MR) due to the decrease of triplet population under an external magnetic field, while the triplet quenching (right side) will produce a positive MR (+MR) under the same circumstances. In our systems, the overall effect on the electric current appears to be a combination of or a competition between these two processes. In the system without an F-SAM, the triplet−polaron scattering process dominates and thus −MR occurs.[15,44,47] In contrast, the triplet quenching and dissociation near the Au electrode becomes more dominant when an F-SAM is inserted due to charge accumulation. This produces a +MR, a sign reversal of MR relative to the samples without an F-SAM.[15,44,47]

In the same manner, the triplet−polaron interaction mechanism determines the behavior of the MR in the Au/TPD/Alq$_3$/Ca systems at lower bias voltages (<2.5 V), thus reversing the polarity of MR when an F-SAM is inserted as shown in Figure 2. However, in the higher voltage regime, the $\sqrt{B}$ dependence begins to dictate the behavior of MR as we mentioned earlier (Figure 2). On the basis of our experimental observations, we believe that the $\sqrt{B}$ behavior of MR in our systems originates from the blended area near the TPD/Alq$_3$ interface due to charge accumulation. It is likely that charge transfer pairs accumulate near the TPD/Alq$_3$ interface consisting of electrons provided by Alq$_3$ and holes by TPD. Since the electron and hole are in different materials or radicals, they may have different g-factors,[12,13,49] and the separation of their pair in the TPD/Alq$_3$ blended area can be large enough for their exchange energy to be disregarded.[29,50] In this case, it was theoretically suggested that the relative recombination rate for electron−hole pairs is proportional to $-(\Delta g \beta B)^{1/2}$ at high magnetic field, where $\Delta g = |g_e - g_h|$, where g_e is the g-factor for electrons, g_h is for holes, and β is Bohr magneton.[29] Because less recombination increases the electric current, if they are directly proportional to each other, the relative

current change by magnetic field or MR should be negative and proportional to $\sqrt{B}$ in high magnetic fields. This effect becomes stronger in the higher current regime because more electron−hole pairs become available for recombination due to higher charge accumulation near the TPD/Alq$_3$ interface. Thus, in lower magnetic fields or with low current, non-Lorentzian-type MR curves with either a negative (without an F-SAM) or a positive (with an F-SAM) polarity can be obtained by random hyperfine field, but in higher magnetic fields with high current, Zeeman interaction with different g-factors becomes dominant, causing $\sqrt{B}$-type negative MR. (One should note that a gyromagnetic difference can produce a different MR behavior in another situation suggested by recent reports.[12,27]) The system with an F-SAM showed two pronounced capacitance humps in Figure 3c; the first hump most likely corresponds to charge carrier accumulation near the Au electrode which will cause organic +MR induced by triplet dissociation. We attribute the second hump to charge carrier accumulation at the TPD/Alq$_3$ interface where the $\sqrt{B}$ dependence is dominant thus producing −MR. This pronounced hump implies that spinodal dewetting of the relatively thin TPD (10 nm) induced by the F-SAM gives rise to a complex interface with a much larger interfacial area between the TPD and the Alq$_3$. The larger charge accumulation at this interface further increases the dominance of the $\sqrt{B}$ behavior.

CONCLUSION

In conclusion, we demonstrated a novel method for tuning the magnitude and sign of organic MR by using SAMs. A fluorinated SAM inserted between a gold electrode and an organic layer influences the morphology of the organic transport material and creates an environment of charge trapping and accumulation near the interface, resulting in the reversal of the polarity of the measured MR. Furthermore, by adding a thin hole transport layer, TPD, to the Alq$_3$-based system with fluorinated SAM, we were able to create a device whose MR polarity is controlled by an external bias voltage. We argue that these phenomena are the outcome of the competition between different magnetic-field-dependent charge carrier transport mechanisms coexisting in these organic devices. We anticipate that our findings will provide a simple yet reliable way of engineering the performance and the functionality of magnetic-field-dependent organic-based systems.

EXPERIMENTAL METHODS

Preparation of Devices and Thin Films. The devices and the thin films in our study were fabricated by using a mechanical shadow mask and thermal evaporation in a vacuum deposition

system with a base pressure of $\approx 7 \times 10^{-6}$ Pa ($\approx 5 \times 10^{-8}$ Torr) at ambient substrate temperature. A sublimed grade 99.995% trace metal basis tris(8-hydroxyquinoline)aluminum (Alq$_3$) and 99% N,N'-bis(3-methylphenyl)-N,N'-diphenylbenzidine (TPD)

were used. The SAMs (both F-SAM and MHA) were prepared by solution immersion method. After the deposition of the SAM, X-ray photoelectron spectroscopy (XPS) and reflection−absorption infrared spectroscopy confirmed successful attachment of the SAM to the Au surface (see Figures S1 and S2). First, a $\approx$100 nm thick Au layer was deposited through a shadow mask on a thermally oxidized ($\approx$300 nm thick SiO_2) silicon substrate, and then, the shadow mask was removed. Subsequently, on the devices, either (1) just Alq_3 was deposited, (2) F-SAM was coated and then Alq_3 was deposited, (3) TPD was deposited and then Alq_3 was deposited, or (4) F-SAM was coated and then TPD/Alq_3 bilayer film was deposited. Alq_3 and TPD thicknesses are $\approx$100 and $\approx$10 nm, respectively. After organic thin film deposition, the mask was placed on the device in a glovebox under Ar gas without exposure to ambient air in order to avoid any oxidation and minimize contamination. All the devices were finalized with the deposition of 20 nm of Ca followed by 100 nm thick Al. The film thickness was monitored during the entire deposition process by a calibrated quartz crystal monitor; the deposition rates were $\approx$0.15 nm/s for Au, $\approx$0.03 nm/s for TPD, $\approx$0.1 nm/s for Alq_3, $\approx$0.2 nm/s for Ca, and $\approx$0.4 nm/s for Al. This process created devices with a cross-bar shape and a $100 \times 100 \,\mu m^2$ junction area. The devices with MHA were prepared by using the same process used for the devices with F-SAM treatment described above. Over 20 devices for each structure were investigated, and they all showed the same electrical and magnetic-field-dependent behaviors described in the main text albeit with slightly different magnitudes. The Alq_3 thin films with different thicknesses (10 and 100 nm) used for the film growth investigation were simultaneously prepared by controlling manually adjustable shutter masks adjacent to the substrate.

Electrical Measurements. The electrical and the MR measurements were carried out in a commercial probe station system under vacuum pressure of $\approx 7 \times 10^{-4}$ Pa ($\approx 5 \times 10^{-6}$ Torr) at room temperature. All the electrical measurements and characterizations were performed in the dark. An external magnetic field was applied parallel to the film plane and perpendicular to the electric current direction as illustrated in Figures 1b and 4a. MR was defined as $MR(B) \equiv (R(B) - R(0))/R(0)$, where $R(B)$ is the electrical resistance at the applied magnetic field B and $R(0)$ is the resistance at zero magnetic field. The low-frequency ac capacitance−voltage (C−V) spectroscopy was performed at the frequencies from 20 to 300 Hz with an ac voltage amplitude of 25 mV as well as 50 mV. Geometrical capacitance C_0 was obtained by averaging out the measured parallel capacitance C_P over bias voltages below zero ($V \leq 0$).

Water Contact Angle Measurements. Sessile water drop contact angles were measured with deionized water landed on our cleaned as well as SAM-treated Au surfaces. All the Au surfaces for the fabricated devices, and the surface and thin film characterization went through the same cleaning steps as follows: (1) 10 min of UV ozone cleaning, (2) ethanol rinse followed by N_2 blow dry, (3) 5 min of UV ozone cleaning, (4) ethanol rinse followed by N_2 blow dry, and (5) deionized ($\approx$18 MΩ) water rinse followed by N_2 blow dry. Any organic contaminants present on the Au surface were expected to be removed after the cleaning process via oxidation by UV ozone cleaning, and the subsequent removal of oxides was done by ethanol and deionized water rinse.

X-ray Diffraction Measurements. Grazing incidence X-ray diffraction measurements were performed at the Stanford Synchrotron Radiation Lightsource (SSRL) Beamline 11-3. The X-ray wavelength was 0.9752 Å, and the incidence angle was 0.12°. The measurements were made in a helium-filled enclosure, and the area detector (MAR2300) was calibrated by using a $LaB6$ standard.

X-ray and Ultraviolet Photoelectron Spectroscopy. X-ray and UV-excited photoelectron spectroscopy measurements were performed in a commercial ultrahigh vacuum system equipped with a hemispherical electron spectrometer with a base pressure of better than 1.33×10^{-7} Pa (1×10^{-9} Torr). Monochromatized Al Kα excitation was used for XPS, and a helium gas discharge lamp was used for UPS operated with He I excitation

(21.22 eV). A bias of −5.5 V was applied to the sample during UPS measurements to clear the work function of the electron spectrometer. The Fermi energy level was referenced from a clean Au surface.

REFERENCES AND NOTES

1. Embracing the Organics World. *Nat. Mater.* **2013**, *12*, 591.
2. Boyen, H.-G.; Ziemann, P.; Wiedwald, U.; Ivanova, V.; Kolb, D. M.; Sakong, S.; Gross, A.; Romanyuk, A.; Büttner, M.; Oelhafen, P. Local Density of States Effects at the Metal−Molecule Interfaces in a Molecular Device. *Nat. Mater.* **2006**, *5*, 394−399.
3. Gundlach, D. J.; Royer, J. E.; Park, S. K.; Subramanian, S.; Jurchescu, O. D.; Hamadani, B. H.; Moad, A. J.; Kline, R. J.; Teague, L. C.; Kirillov, O.; *et al.* Contact-Induced Crystallinity for High-Performance Soluble Acene-Based Transistors and Circuits. *Nat. Mater.* **2008**, *7*, 216−221.
4. Ward, J. W.; Loth, M. A.; Kline, R. J.; Coll, M.; Ocal, C.; Anthony, J. E.; Jurchescu, O. D. Tailored Interface for Self-Patterning Organic Thin-Film Transistors. *J. Mater. Chem.* **2012**, *22*, 19047−19053.
5. Jang, H.-J.; Pernstich, K. P.; Gundlach, D. J.; Jurchescu, O. D.; Richter, C. A. Observation of Spin-Polarized Electron Transport in Alq_3 by Using a Low Work Function Metal. *Appl. Phys. Lett.* **2012**, *101*, 102412−102416.
6. Hu, B.; Yan, L.; Shao, M. Magnetic-Field Effects in Organic Semiconducting Materials and Devices. *Adv. Mater.* **2009**, *21*, 1500−1516.
7. Wagemans, W.; Janssen, P.; Schellekens, A. J.; Bloom, F. L.; Bobbert, P. A.; Koopmans, B. The Many Faces of Organic Magnetoresistance. *SPIN* **2011**, *1*, 93−108.
8. Joo, S.; Kim, T.; Shin, S. H.; Lim, J. Y.; Hong, J.; Song, J. D.; Chang, J.; Lee, H.-W.; Rhie, K.; Han, S. H.; *et al.* Magnetic-Field-Controlled Reconfigurable Semiconductor Logic. *Nature* **2013**, *494*, 72−76.
9. Kalinowski, J.; Cocchi, M.; Virgili, D.; Di Marco, P.; Fattori, V. Magnetic Field Effects on Emission and Current in Alq_3-Based Electroluminescent Diodes. *Chem. Phys. Lett.* **2003**, *380*, 710−715.
10. Francis, T. L.; Mermer, Ö.; Veeraraghavan, G.; Wohlgenannt, M. Large Magnetoresistance at Room Temperature in Semiconducting Polymer Sandwich Devices. *New J. Phys.* **2004**, *6*, 185−192.
11. Hu, B.; Wu, Y. Tuning Magnetoresistance between Positive and Negative Values in Organic Semiconductors. *Nat. Mater.* **2007**, *6*, 985−991.
12. Janssen, P.; Cox, M.; Wouters, S. H. W.; Kemerink, M.; Wienk, M. M.; Koopmans, B. Tuning Organic Magnetoresistance in Polymer−Fullerene Blends by Controlling Spin Reaction Pathways. *Nat. Commun.* **2013**, *4*, 2286−2293.
13. Wang, F. J.; Bässler, H.; Valy Vardeny, Z. Magnetic Field Effects in π-Conjugated Polymer−Fullerene Blends: Evidence for Multiple Components. *Phys. Rev. Lett.* **2008**, *101*, 236805−236808.

14. Kang, H.; Lee, I.-J.; Yoon, C. S. Sign Change in the Organic Magnetoresistance of Tris(8-hydroxyquinolinato)Aluminum upon Annealing. *Appl. Phys. Lett.* **2012**, *100*, 073302–073305.

15. Desai, P.; Shakya, P.; Kreouzis, T.; Gillin, W. P. The Role of Magnetic Fields on the Transport and Efficiency of Aluminum Tris(8-hydroxyquinoline) Based Organic Light Emitting Diodes. *J. Appl. Phys.* **2007**, *102*, 073710–073714.

16. Kobayashi, S.; Nishikawa, T.; Takenobu, T.; Mori, S.; Shimoda, T.; Mitani, T.; Shimotani, H.; Yoshimoto, N.; Ogawa, S.; Iwasa, Y. Control of Carrier Density by Self-Assembled Monolayers in Organic Field-Effect Transistors. *Nat. Mater.* **2004**, *3*, 317–322.

17. Wünsche, J.; Tarabella, G.; Bertolazzi, S.; Bocoum, M.; Coppedè, N.; Barba, L.; Arrighetti, G.; Lutterotti, L.; Iannotta, S.; Cicoirae, F.; *et al.* The Correlation between Gate Dielectric, Film Growth and Charge Transport in Organic Thin Film Transistors: The Case of Vacuum-Sublimed Tetracene Thin Films. *J. Mater. Chem. C* **2013**, *1*, 967–976.

18. Lee, W. H.; Cho, J. H.; Cho, K. Control of Mesoscale and Nanoscale Ordering of Organic Semiconductors at the Gate Dielectric/Semiconductor Interface for Organic Transistors. *J. Mater. Chem.* **2010**, *20*, 2549–2561.

19. Ma, H.; Yip, H.-L.; Huang, F.; Jen, A. K.-Y. Interface Engineering for Organic Electronics. *Adv. Funct. Mater.* **2010**, *20*, 1371–1388.

20. Akkerman, H. B.; Blom, P. W. M.; de Leeuw, D. M.; de Boer, B. Towards Molecular Electronics with Large-Area Molecular Junctions. *Nature* **2006**, *441*, 69–72.

21. Love, J. C.; Estroff, L. A.; Kriebel, J. K.; Nuzzo, R. G.; Whitesides, G. M. Self-Assembled Monolayers of Thiolates on Metals As a Form of Nanotechnology. *Chem. Rev.* **2005**, *105*, 1103–1169.

22. DiBenedetto, S. A.; Facchetti, A.; Ratner, M. A.; Marks, T. J. Molecular Self-Assembled Monolayers and Multilayers for Organic and Unconventional Inorganic Thin-Film Transistor Applications. *Adv. Mater.* **2009**, *21*, 1407–1433.

23. Zhu, L.; Tang, H.; Harima, Y.; Yamashita, K.; Asob, Y.; Otsubo, T. Enhanced Hole Injection in Organic Light-Emitting Diodes Consisting of Self-Assembled Monolayer of Tripod-Shaped π-Conjugated Thiols. *J. Mater. Chem.* **2002**, *12*, 2250–2254.

24. Nüesch, F.; Rotzinger, F.; Si-Ahmed, L.; Zuppiroli, L. Chemical Potential Shifts at Organic Device Electrodes Induced by Grafted Monolayers. *Chem. Phys. Lett.* **1998**, *288*, 861–867.

25. Mermer, Ö.; Veeraraghavan, G.; Francis, T. L.; Sheng, Y.; Nguyen, D. T.; Wohlgenannt, M.; Köhler, A.; Al-Suti, M. K.; Khan, M. S. Large Magnetoresistance in Nonmagnetic π-Conjugated Semiconductor Thin Film Devices. *Phys. Rev. B* **2005**, *72*, 205202–205213.

26. Majumdar, S.; Majumdar, H. S.; Aarnio, H.; Vanderzande, D.; Laiho, R.; Österbacka, R. Role of Electron–Hole Pair Formation in Organic Magnetoresistance. *Phys. Rev. B* **2009**, *79*, 201202–201205.

27. Schellenkens, A. J.; Wagemans, W.; Kersten, S. P.; Bobbert, P. A.; Koopmans, B. Microscopic Modeling of Magnetic-Field Effects on Charge Transport in Organic Semiconductors. *Phys. Rev. B* **2011**, *84*, 075204–075215.

28. Kawabata, A. Theory of Negative Magnetoresistance in Three-Dimensional Systems. *Solid State Commun.* **1980**, *34*, 431–432.

29. Tanimoto, Y.; Hayashi, H.; Nagakura, S.; Sakuragi, H.; Tokumaru, K. The External Magnetic Field Effect on the Singlet Sensitized Photolysis of Dibenzoyl Peroxide. *Chem. Phys. Lett.* **1976**, *41*, 267–269.

30. Ahn, J.; Chung, D.-H.; Lee, J.-U.; Lee, G.-S.; Song, M.-J.; Lee, W.-J.; Han, W.-K.; Kim, T. W. Equivalent-Circuit Analysis of Organic Light-Emitting Diodes by Using the Frequency-Dependent Response of an ITO/Alq$_3$/Al Device. *J. Korean. Phys. Soc.* **2005**, *46*, 546–550.

31. Shrotriya, V.; Yang, Y. Capacitance–Voltage Characterization of Polymer Light-Emitting Diodes. *J. Appl. Phys.* **2005**, *97*, 054504–054509.

32. Weingarten, M.; Slawinski, M.; Urbain, F.; Fahle, D.; Bertram, D.; Heuken, M.; Kalisch, H.; Vescan, A. Characterization of Charge Carrier Injection in Organic and Hybrid Organic/Inorganic Semiconductor Devices by Capacitance–Voltage Measurements. *Proc. SPIE* **2012**, *8476*, 8476H1–8476H7.

33. Nowy, S.; Ren, W.; Wagner, J.; Weber, J. A.; Brütting, W. Impedance Spectroscopy of Organic Hetero-Layer OLEDs as a Probe for Charge Carrier Injection and Device Degradation. *Proc. SPIE* **2009**, *7415*, 74150G1–74150G11.

34. Garcia-Belmonte, G.; Bolink, H. J.; Bisquert, J. Capacitance–Voltage Characteristics of Organic Light-Emitting Diodes Varying the Cathode Metal: Implications for Interfacial States. *Phys. Rev. B* **2007**, *75*, 085316–085323.

35. Sharma, A.; Kumar, P.; Singh, B.; Chaudhuri, S. R.; Ghosh, S. Capacitance–Voltage Characteristics of Organic Schottky Diode with and without Deep Traps. *Appl. Phys. Lett.* **2011**, *99*, 023301–023303.

36. Gommans, H. H. P.; Kemerink, M.; Janssen, R. A. J. Negative Capacitances in Low-Mobility Solids. *Phys. Rev. B* **2005**, *72*, 235204–235209.

37. Bloom, F. L.; Wagemans, W.; Kemerink, M.; Koopmans, B. Separating Positive and Negative Magnetoresistance in Organic Semiconductor Devices. *Phys. Rev. Lett.* **2007**, *99*, 257201–257204.

38. Sehgal, A.; Ferreiro, V.; Douglas, J. F.; Amis, E. J.; Karim, A. Pattern-Directed Dewetting of Ultrathin Polymer Films. *Langmuir* **2002**, *18*, 7041–7048.

39. Pacifico, J.; Endo, K.; Morgan, S.; Mulvaney, P. Superhydrophobic Effects of Self-Assembled Monolayers on Micropatterned Surface: 3-D Arrays Mimicking the Lotus Leaf. *Langmuir* **2006**, *22*, 11072–11076.

40. Kaake, L. G.; Barbara, P. F.; Zhu, X.-Y. Intrinsic Charge Trapping in Organic and Polymeric Semiconductors: A Physical Chemistry Perspective. *J. Phys. Chem. Lett.* **2010**, *1*, 628–635.

41. Veres, J.; Ogier, S. D.; Leeming, S. W.; Cupertino, D. C.; Khaffaf, S. M. Low-*K* Insulators as the Choice of Dielectrics in Organic Field-Effect Transistors. *Adv. Funct. Mater.* **2003**, *13*, 199–204.

42. Ahmad, S. N.; Shaheen, S. A.; Rao, S. G.; Magnan, D.; Strouse, G. F. Effect of Polarity of Self-Assembled Monolayers on Morphology and Magnetic Properties of a Deposited Magnetic Material. *J. Appl. Phys.* **2008**, *103*, 07B507–07B509.

43. Lv, Z.; Wang, J.; Deng, L.; Chen, G. Preparation and Characterization of Covalently Binding of Rat Anti-Human IgG Monolayer on Thiol-Modified Gold Surface. *Nanoscale Res. Lett.* **2009**, *4*, 1403–1408.

44. Desai, P.; Shakya, P.; Kreouzis, T.; Gillin, W. P.; Morley, N. A.; Gibbs, M. R. J. Magnetoresistance and Efficiency Measurements of Alq$_3$-Based OLEDs. *Phys. Rev. B* **2007**, *75*, 094423–094427.

45. Bergeson, J. D.; Prigodin, V. N.; Lincoln, D. M.; Epstein, A. J. Inversion of Magnetoresistance in Organic Semiconductors. *Phys. Rev. Lett.* **2008**, *100*, 067201–067204.

46. Bobbert, P. A.; Nguyen, T. D.; van Oost, F. W. A.; Koopmans, B.; Wohlgenannt, M. Bipolaron Mechanism for Organic Magnetoresistance. *Phys. Rev. Lett.* **2007**, *99*, 216801–216804.

47. Ern, V.; Merrifield, R. E. Magnetic Field Effect on Triplet Exciton Quenching in Organic Crystals. *Phys. Rev. Lett.* **1968**, *21*, 609–611.

48. Yu, J.; Lammi, R.; Gesquiere, A. J.; Barbara, P. F. Singlet–Triplet and Triplet–Triplet Interaction in Conjugated Polymer Single Molecules. *J. Phys. Chem. B* **2005**, *109*, 10025–10034.

49. Batagin-Neto, A.; Gómez, J. A.; Castro, F. A.; Nüesch, F.; Zuppiroli, L.; Graeff, C. F. O. Exciton Formation in Dye Doped OLEDs Using Electrically Detected Magnetic Resonance. *Proc. SPIE* **2011**, *8333*, 83331B1–83331B7.

50. Kaptein, R. Chemically Induced Dynamic Nuclear Polarization. VIII. Spin Dynamics and Diffusion of Radical Pairs. *J. Am. Chem. Soc.* **1972**, *94*, 6251–6262.